

Nanosecond pulsed barrier discharge in argon for various frequencies and theoretical analysis of 2p states density ratios for E/N determination

L. Kusýn^{1,*}, A. P. Jovanović^{2,*}, D. Loffhagen²,
M. M. Becker^{2,☉} and T. Hoder^{1,☉}

¹Department of Plasma Physics and Technology, Faculty of Science, Masaryk University, Kotlářská 2, 61137 Brno, Czech Republic

²Leibniz Institute for Plasma Science and Technology, Felix-Hausdorff-Str. 2, 17489 Greifswald, Germany

*These authors contributed equally to this work and share first authorship.

☉Corresponding authors.

E-mail: hoder@physics.muni.cz, markus.becker@inp-greifswald.de

Abstract.

Nanosecond pulsed barrier discharges in atmospheric pressure argon are simulated using spatially one- and two-dimensional fluid-Poisson models using the reaction kinetics model presented by Stankov *et al.* [1], which considers all ten argon 2p states (Paschen notation) separately. The very first (single) discharge and repetitive discharges with frequencies from 5 kHz to 100 kHz are considered and a semi-automated procedure is utilized to find appropriate 2p states for electric field determination using an intensity ratio method. The proposed method is based on a time-dependent collisional-radiative model enabling a sub-nanosecond plasma diagnostics, it links the 2p state density ratios to the reduced electric field strength E/N by quantifying the excitation rate coefficients and by computing 2p states' effective lifetimes from the fluid model simulation. The semi-automated procedure identifies several candidates for determination of E/N from given temporal profiles of the 2p state densities. Different approaches for effective lifetime determination are tested and applied also to measured data. The influence of radial and axial 2p state density integration on the intensity ratio method is discussed. The above mentioned models and procedures result in a flexible theory-based methodology applicable for development of new diagnostic techniques.

1. Introduction

The electric field is a fundamental parameter for gas discharges and generated transient plasmas. The detailed knowledge of this physical quantity is important, for detailed understanding of studied plasmas and for validation of theoretical models focused on the plasma dynamics or chemical kinetics. The determination of the electric field parameter is therefore a crucial task and a variety of methods is available [2] also for argon plasmas, which are of high interest in various applications [3–7]. For example, laser-induced fluorescence-dip spectroscopy [8] was used to determine the electric field development in lower pressure argon [9]. The widely applied electric-field-induced second harmonics (EFISH) based laser spectroscopy was recently used for investigation of plasma jets [10], too. Optical emission spectroscopy (OES) based Stark shift measurements enabled the experimental determination of the electron temperature, which is closely related to the electric field, in an atmospheric pressure argon micro-discharge in [11]. A collisional-radiative model (CRM) in combination with OES measurements was used to determine the electron temperature in low pressure plasma using the line-ratio method [12]. Line-ratio (a spectral line intensity ratio) method was recently introduced by Dyatko *et al.* [13] for the ionization wave electric field estimation in low pressure argon discharges. Nevertheless, the spatiotemporally highly resolved determination of the reduced electric field E/N in atmospheric pressure argon plasma using an OES method, similar to what is known for air discharges [14–17], is not available. Here, E is the electric field strength and N denotes the number density of the background gas.

Argon barrier discharges are widely used in multiple arrangements, exhibiting broad values of parameters (electric field, electron number density, etc.) under different experimental conditions (applied voltage, frequency, wave form, etc.). It is therefore desirable to have a method which is able to access the E/N under most of the assumed condition. For example, in the case of nanosecond pulsed applied voltage operation at different pulse frequencies. It is known that the discharge mechanisms can vary significantly, as it was shown e.g. for nitrogen-oxygen mixtures in [18] or as it is apparent comparing the low frequency barrier discharge with a high frequency

mode [19] or even in a modulated dual-frequency mode [20, 21]. The intensity ratio diagnostic method of such discharges, based on simple CRM and using an OES experiment, could be related to the emission from radiative states of the 2p manifold of argon as it usually dominates the argon barrier discharge spectra. As the excitation energy thresholds for 2p states differ relatively only slightly, their use for the intensity ratio method is expected to be challenging. Nevertheless, the experimental results presented in [22] report clearly that 2p state intensity ratios are sensitive to the spatiotemporal dynamics of the nanosecond pulsed discharge, if recorded with high sensitivity and high temporal resolution.

In this article, we present a methodology how to approach the problem: by semi-automated analysis of a large amount of data obtained from numerical simulations using a time- and space-dependent fluid-Poisson modelling approach. With this, we investigate the possibility to use the argon atomic line intensity ratio method under above described conditions. The theoretical investigation provides insights into the sensitivity of the selected reaction kinetic processes for the given discharge conditions, which is also essential to quantify the limitations of the suggested line intensity ratio method. It is worth noting that we evaluate the intensity ratio method using a time-dependent CRM, enabling possible sub-nanosecond experimental insight into argon plasmas, if fast detectors are used. The introduced and utilized methodology for intensity ratio method investigation can be applied also to other gas mixtures under various conditions, e.g. for E/N determination in planetary atmospheres [23] or in plasmas for gas conversion [24].

The mentioned intensity ratio methods for electric field determination are designed to identify the contribution of relaxed electron ensemble given by the electron energy distribution function to two excitation processes. This method has previously been used for air plasmas [2, 14, 16]. The named excitation processes populate two radiative states having different energy thresholds which are responsible for the detected optical emission. One of the main requirements of the method is that both excitation processes start from the same lower state, typically direct electron impact excitation from the ground state of the atom or molecule of the background gas. This condition is fulfilled for weakly ionised low-frequency plasmas and/or under conditions with very strong

collisional quenching, as it is the case in air. Under such conditions, nitrogen metastable states' densities decrease very fast due to the effective quenching by oxygen after each discharge and cannot contribute significantly via stepwise excitation processes as they are basically not present. Apparently, this condition cannot be fulfilled for repetitive or long-duration discharges in pure argon or pure nitrogen [1, 25–27], where densities of metastable states become significant. To overcome this issue one needs to determine the metastable density and take the stepwise excitation process into account in the CRM related to the intensity ratio method [28].

A second possibility is to find two radiative states whose population processes are not sensitive to the presence of the metastable states so that stepwise excitation can be neglected, at least for some conditions. This second possibility is theoretically more demanding yet also more experiment-friendly, as it does not require the knowledge of the metastable states' density in the studied plasma (which needs to be additionally measured). In this article, we follow this second direction.

An important part of intensity ratio methods for electric field determination is the knowledge of the dependence of the intensity ratio $R(E/N)$ on the reduced electric field. Theoretically, the ratio of two reaction rates has to be determined and the corresponding simple CRM has to be well founded, as it was done for air using sensitivity analysis and uncertainty quantification in [29]. For plasmas in air or nitrogen, the $R(E/N)$ dependence was obtained both experimentally and theoretically e.g. in [2, 29–32] and references therein. Paris *et al.* [30] determined the $R(E/N)$ dependence experimentally for air. In all these cases, the procedure is based on Townsend discharges with reaction kinetics in equilibrium. The Townsend discharge is a steady-state discharge with different properties if compared with streamer discharges, where the method is usually used. The exception is to additionally modify the dependence of Paris *et al.* [30] as suggested in [16, 31, 33, 34]. Such modified curve was used for diagnostics of streamer or nanosecond pulsed discharges [17, 35] and is well within the uncertainty interval discussed in [29, 31]. To overcome the issue of the $R(E/N)$ dependence coming from the equilibrated steady-state Townsend discharge, the method may be developed and studied also in a time-dependent case by a theoretical means (see also [15]), i.e. within an argon barrier discharge simulation using an appropriate reaction kinetics model (RKM, see [1] for example) in fine spatiotemporal resolution, as we do in the present manuscript.

We investigate the possibility to develop an intensity ratio method for atmospheric pressure argon

plasmas using numerical simulations of a barrier discharge. Up to now, we have developed a solid theoretical foundation by creating an enhanced reaction kinetics model (see [1]) used for spatially one-dimensional (1D) modelling, by developing a spatially two-dimensional (2D) fluid model for case-specific computer simulations (see [27, 36, 37]) and by performing first 2p spectra measurements with sufficiently high temporal and spatial resolution to establish the link to the experiment (see [22]). Here, a dielectric barrier discharge in an asymmetrical arrangement (only one electrode is covered by a dielectrics) and operated by nanosecond pulsed voltage waveform at various frequencies is studied using numerical simulations. As a result, we have direct theoretical access to the development of the number densities of all important states and therefore to the sub-nanosecond spectra of the discharge in the most intense spectral region between 650 nm and 900 nm. Using a semi-automated procedure, we attempt to identify the most suitable 2p states for the intensity ratio method based on the analysis of the theoretical data and apply these findings to the experimental results.

The manuscript is structured in the following way. In section 2, the modelling procedure is described, including the RKM [1] with necessary reference to our previous work. In section 3, the results are presented and discussed. Including the discharge dynamics under the nanosecond pulsed voltage waveform at different frequencies in subsection 3.1. In such way, the studied discharge is well prepared for the analysis of the 2p states' kinetics in subsection 3.2, where the intensity ratio method is investigated for all combinations of 2p state ratios. In subsection 3.3, the effects of the density/signal integration are discussed, which are of importance for the laboratory experiment providing line-of-sight integrated profiles. Furthermore, a selected 2p state intensity ratio is analyzed for the measured data and compared to the results of the fluid simulations. In the final section, the presented work is concluded and summarized.

2. Discharge arrangement and modelling procedure

Figure 1 shows the discharge arrangement together with typical voltage and current waveforms in the repetitive regime. The electrode arrangement considered in the simulations was the same as in previous experimental and theoretical investigations [22, 27, 38]. An asymmetric volume barrier discharge with one electrode covered by the alumina dielectric (96% purity Al_2O_3) is studied. The electrodes are made of stainless steel. The gas gap is 1.5 mm,

the dielectric thickness is 0.5 mm (in [38], wrong value of the dielectric thickness of 1 mm) is given for the same setup, the dielectric's permittivity is $\epsilon_r = 9$, and the radius of the electrode surfaces is 2 mm. Later in this article, the developed theoretical approach is applied to the experimental data obtained in [22]. Those experiments were done under the following conditions: The electrodes are in the sealed glass chamber evacuated to high vacuum (10^{-5} mbar), heated to 700 K for several hours (baked out to reduce impurities) and then filled with argon gas of high purity of 99.9999% to atmospheric pressure. In the previous work [22], the emission in the pulsed barrier discharge was investigated by photomultipliers PMC-100-20 and PMC-100-4 and processed by time-correlated single photon counting module SPC-150 from Becker and Hickl GmbH. The voltage and current measurements were conducted by P6015A voltage probe (Tektronix) and current transformer CT-2 (Tektronix), respectively. Electrical characteristics were then captured by a high-definition oscilloscope Keysight DSO-2 204A. More details, parameters and a schematic of the experimental setup can be found in [22].

The time- and space-dependent fluid-Poisson model used in the present work to simulate the introduced pulsed barrier discharge is described in [36, 39]. Numerical calculations were performed for the given experimental conditions and different frequencies of the applied voltage. The applied voltage amplitudes were the same for all simulations as shown in Figure 1(c and (d)), i.e. approx. 5.6 kV for the nanosecond pulse. The rise time of the applied voltage pulse was about 40 ns. The fluid-Poisson model was solved in 1D (in further text denoted as 1D model) and 2D geometry (denoted as 2D model). The 2D model considers the entire geometry shown in Figure 1(a) and (b). The 1D modelling studies were performed along the discharge symmetry axis at $r = 0$ mm illustrated by the grey dashed line in Figure 1(b), neglecting radial effects.

The voltage was applied to the metal electrode (i.e. the electrode without the dielectric coverage, see the lower part in Figure 1(a)) with a repetition frequency of 5, 10, 20, 50 and 100 kHz, respectively. The other electrode was grounded. For repetitive discharges described by the 1D model, the modelling was performed until a quasi-periodic state was reached (typically ten periods). Typical current and voltage waveforms after reaching the periodic regime are shown in Figures 1(c) and (d). Here, the memory voltage is the voltage drop across the dielectric layer, which is determined by subtracting the gap voltage (voltage drop across the gas gap) from the applied voltage. The 2D model was used to describe only the very first discharge until the streamer reached the cathode.

It was used to clarify the influence of radial effects and particularly the effect of line-of-sight integration of measured light emission signals (the radiative state densities) from the discharge. The model calculations in 2D were limited to the first discharge due to the high computation cost including the full reaction kinetics scheme detailed in [1].

The fluid-Poisson model in 1D and 2D comprises the same set of particle balance equations, Poisson's equation and the electron energy balance equation. An additional balance equation for the surface charge density σ was solved at the plasma-dielectric interface and used as boundary condition for the Poisson equation [27]. More details about the model implementation and the numerical procedure used to solve the equations can be found in [36].

Table 1. List of argon species considered in the RKM.

Index	Species	Energy level [eV]
1	Ar[1p0]	0
2	Ar[1s5]	11.55
3	Ar[1s4]	11.62
4	Ar[1s3]	11.72
5	Ar[1s2]	11.82
6	Ar[2p10]	12.91
7	Ar[2p9]	13.08
8	Ar[2p8]	13.09
9	Ar[2p7]	13.15
10	Ar[2p6]	13.17
11	Ar[2p5]	13.27
12	Ar[2p4]	13.28
13	Ar[2p3]	13.30
14	Ar[2p2]	13.33
15	Ar[2p1]	13.40
16	Ar*[hl]	13.84
17	Ar ⁺	15.76
18	Ar ₂ [*] [³ Σ _u ⁺ , v = 0]	9.76
19	Ar ₂ [*] [¹ Σ _u ⁺ , v = 0]	9.84
20	Ar ₂ [*] [³ Σ _u ⁺ , v ≫ 0]	11.37
21	Ar ₂ [*] [¹ Σ _u ⁺ , v ≫ 0]	11.45
22	Ar ₂ [*]	14.50

The reactions kinetics model (RKM) considers the electron component, 22 heavy particle species and about 400 collision and radiation processes. The list of considered heavy particle species as well as their energy levels is given in Table 1. Further details regarding the reaction kinetics are represented in [1]. This reaction kinetics model was designed for the analysis of the electrical characteristics and for the description of production and loss channels of the excited species in gas discharge plasmas in the range from low to atmospheric pressure. The 2p states are here of special importance due to their dominant contribution to the optical emission spectrum. Each of the 2p states is described using the following equation:

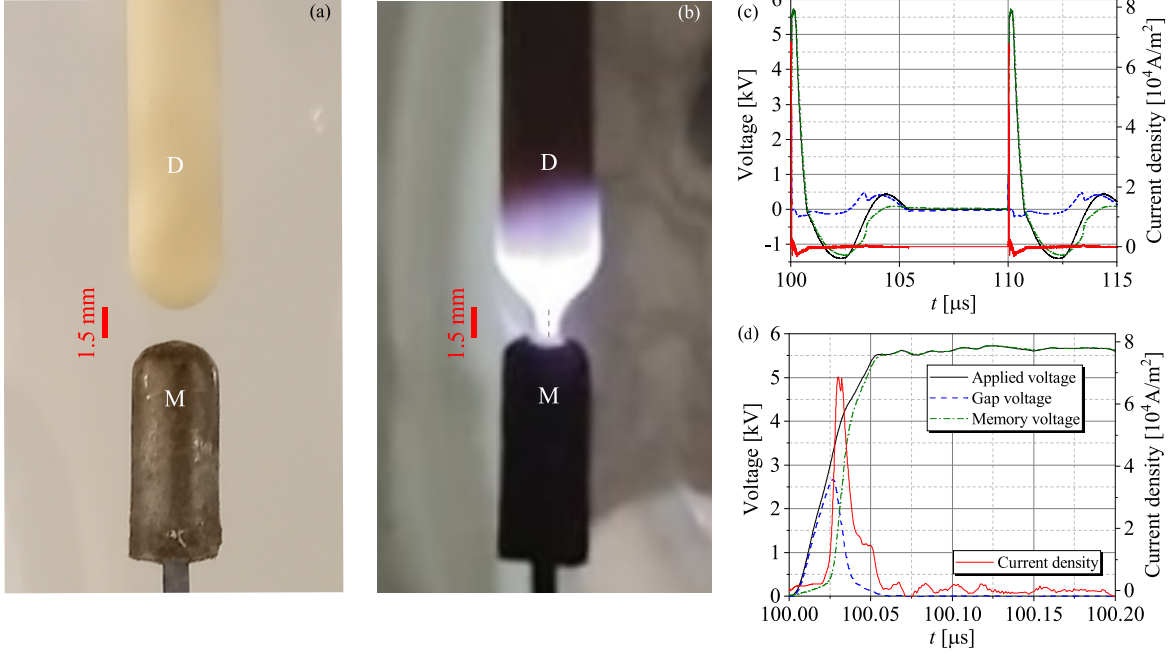


Figure 1. Illustration of the asymmetric barrier discharge in atmospheric pressure argon showing (a) the photograph of the discharge geometry without discharge, (b) with discharge, and (c) and (d) the temporal evolution of the current and voltage after reaching periodic regime resulting from the 1D simulation. The metal electrode and the dielectric surface are denoted as M and D, respectively, in (a) and (b). The grey dashed line in (b) illustrates the axial cut at which the 1D model was used. The part (d) zooms into the electrical parameters of the discharge event at the rising slope of the applied voltage. The rise time (10 to 90%) of the voltage pulse is approximately 40 ns.

$$\begin{aligned}
\frac{dn_{2p_i}}{dt} = & \left[n_e \left\{ n_g k_{g,2p_i} \right\} \right]_I + \left[n_e \left\{ \sum_{j=2}^5 n_{1s_j} k_{1s_j,2p_i} \right\} \right]_{II} \\
& + \left[n_e \left\{ \sum_{m,m \neq i} n_{2p_m,2p_i} k_{2p_m,2p_i} \right\} \right]_{III} + \left[n_e \left\{ n_{hl} k_{hl,2p_i} \right\} \right]_{IV} + \left[n_e \left\{ n_{Ar_2^+} k_{Ar_2^+,2p_i} \right\} \right]_V \\
& - \left[n_e n_{2p_i} \left\{ \sum_{j=2}^5 k_{2p_i,1s_j} \right\} \right]_{VI} - \left[n_e n_{2p_i} \left\{ \sum_{m,m \neq i} k_{2p_i,2p_m} \right\} \right]_{VII} - \left[n_e n_{2p_i} \left\{ k_{2p_i,g} + k_{2p_i,hl} + k_{2p_i,ion} \right\} \right]_{VIII} \\
& + \left[n_g \sum_{m,m \neq i} \left\{ k_{2p_m,2p_i} (T_g) n_{2p_m} - k_{2p_i,2p_m} (T_g) n_{2p_i} \right\} \right]_{IX} - \left[n_g \sum_{j=2}^5 \left\{ k_{2p_i,1s_j} (T_g) n_{2p_i} \right\} \right]_X \\
& + [n_{hl} A_{hl,2p_i}]_{XI} - \left[n_{2p_i} \sum_{j=2}^5 \left\{ A_{2p_i,1s_j} \right\} \right]_{XII}
\end{aligned} \tag{1}$$

where n_{2p_i} is the density of the given 2p state with i ranging from 1 to 10, n_g and n_e are the ground gas (Ar[1p₀]) and electron density, respectively, E/N is the reduced electric field, $k_{g,2p_i}$ is rate coefficient for excitation of the $2p_i$ state from the ground state and similarly for other collision processes contributing to the population or depopulation of the respective $2p_i$ state. A_{hl} denotes the Einstein coefficient of higher lying states hl (lumped for all states energetically higher than the $2p_1$ state, see [1]), which are here lumped into one state. The rate equation includes gain processes from direct electron impact excitation from ground state (I), stepwise excitation from 1s states (II), excitation and de-excitation from other 2p states (III), de-excitation from higher lying state (IV) and electron-ion recombination (V). It further includes loss processes from electron impact de-excitation to 1s states (VI), excitation and de-excitation to other 2p states (VII) and to ground and higher lying states as well as stepwise ionization (VIII). Equation (1) also includes heavy-particle quenching processes from and to upper and lower 2p states (gain and loss) (IX), depopulation due to quenching processes to 1s states (X), population due to radiative de-excitation of the higher lying state (XI) and radiative de-excitation to 1s states (XII) described by the Einstein coefficients $A_{2p_i,1s_j}$. Referring to the last term in the equation, this RKM allows to monitor the densities of relevant radiative excited species responsible for the strong lines in argon spectra during the discharge, as observed in experiments [22, 25, 40].

To allow proper comparison of the very first discharge events for the 1D and 2D model, the same initial number density of particle species and mean electron energy were set in both cases. Namely, the initial density of excited argon atoms and molecules and positive argon ions was set to 10^9 m^{-3} and the initial density of electrons was set to $2 \times 10^9 \text{ m}^{-3}$ to assure quasi-neutral initial conditions. An initial mean electron energy of 1.5 eV was assumed in the gap and the gas temperature was fixed at 300 K for all model calculations.

3. Results

In this section, we present the results of numerical simulations, first for the 2D geometry where we describe the data treatment for investigation of the effect of radial or axial signal integration. Second, for the 1D geometry where the discharge dynamics for different frequencies is presented together with quantitative description of all parameters (E/N , streamer velocity, density of electrons, metastables and 2p states) important for development and validation of the CRM for the intensity ratio method. Further,

the simple CRM for the intensity ratio method is described together with all its components and with care to evaluation of the effective lifetimes of the utilized 2p states. Finally, the semi-automated method is presented and used to evaluate the data from 1D simulations for all investigated frequencies and a comparison with the experimental results is made.

As a brief introduction to the dynamics of the nanosecond pulsed barrier discharge and to illustrate the sampling procedure, the results of the 2D modelling are shown first. Figure 2 shows the voltage and current waveforms together with the spatial distribution of the $2p_4$ state density in the streamer at the time of 40.6 ns calculated by means of the 2D model for the first discharge event. That is the calculations start at $t = 0$. The time instant of 40.6 ns is highlighted by a dashed vertical line also in Fig. 2(a). The discharge starts with increased current to the level of about 15 mA. This is due to the displacement current and initial electron multiplication in the gas gap. After the local free charge density crosses a certain threshold, the streamer starts and propagates towards the cathode. This is reflected by a rapid increase of the discharge current. In this work, we are interested in this initial phase of streamer propagation. After the streamer impacts onto the cathode the transient glow discharge plasma is created and with the accumulation of surface charges on the dielectrics the discharge is quenched. The discharge development after the streamer impact onto the dielectric was studied in detail for the same configuration in a sine-driven single-filament atmospheric-pressure DBD in [27, 37].

Three horizontal lines drawn in Figure 2(b) denote positions which were selected to analyse the detailed reaction kinetics, dominantly of the 2p states. Experimentally, the spectra originating from 2p radiative states were measured for nanosecond pulsed discharge at the selected positions of 0.44, 0.88 and 1.24 mm as in [22]. Here, additional positions were selected at 1.0 and 1.48 mm.

The results of the 1D and 2D model were sampled for post-processing using a spatial resolution of $2 \mu\text{m}$ along the discharge axis and a temporal resolution of 20 ps. From this data set, the evaluation was performed at the positions $z = 0.88, 1.00, 1.24$ and 1.48 mm. The data evaluated from a single point of the discharge axis ($r = 0 \text{ mm}$) are described as “point data” in the following.

In the experiment, the discharge filament is typically projected perpendicularly onto the monochromator slit, which is then by its opening (usually few tens of microns) defining the axial resolution of the measurement, typically $30 \mu\text{m}$. The 1D model does not deliver the radial structure of the discharge. In addition to point data, results of particle number densities

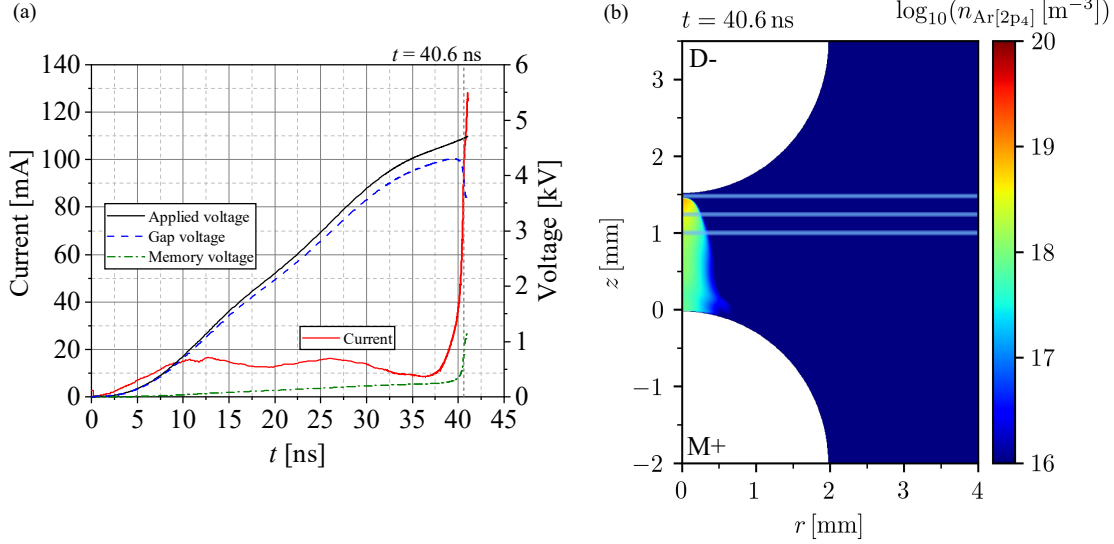


Figure 2. Illustration of (a) the temporal evolution of the current and voltage and (b) the spatial distribution of $2p_4$ state density at a given time calculated using the 2D model. The metal electrode and the dielectric surface are denoted as M and D, respectively, where ‘+’ sign indicates the temporary anode and ‘-’ the temporary cathode. The moment of the streamer arrival at the cathode at $t = 40.6$ ns was taken for an illustration of the streamer spatial profile. The three shown horizontal lines at $z = 1.0$, 1.24 and 1.48 mm highlight the positions for more detailed investigations and for comparison with measured data from [22].

axially integrated over $30 \mu\text{m}$ (summation over 15 cells on the discharge axis) are shown. Moreover, the particle number densities have been integrated in axial and radial direction using the 2D modelling results to reproduce the complete signal input to the detector as in the experiment. These results are referred to as “integrated data” in the following. The integration of the particle number densities obtained from the 2D model was done using the equation

$$n_{p,int} = 2\pi \int_0^{R_d} \int_{z_1}^{z_2} n_p r dr dz, \quad (2)$$

where $n_{p,int}$ are integrated densities n_p of species p , z_1 and z_2 are coordinates at the z -axis, where $\Delta z = z_2 - z_1 = 30 \mu\text{m}$, and $R_d = 4$ mm is the radius of the computational domain.

In following subsections, we investigate the discharge dynamics for different frequencies and the $2p$ states suitable for the intensity ratio method.

3.1. Discharge dynamics for different frequencies

The asymmetric barrier discharge in atmospheric pressure argon was simulated for frequencies ranging from 5 to 100 kHz using the 1D model. Modelling results of that frequency variation are shown in Figure 3, where the current densities j (a), magnitudes $|E|/N$ of the reduced electric field (b) and electron number densities n_e (c) are presented.

Apparently the current density peaks at the rising slope of the nanosecond voltage pulse, where a strong discharge takes place. It is apparent from Figure 3(a)

that the maximum current density decreases with increasing frequency. Additionally, discharge with a significantly smaller peak current density and of considerably longer duration takes place on the falling slope of the applied voltage pulse, see Figure 1. Such an event is a result of the discharging of the residual charge left on the dielectric surface during the rising slope (see also [41]). Note that this is an asymmetric barrier discharge and thus also the secondary electron emission coefficient or the local influence of the accumulated surface charge are different for the respective surface material (metal or dielectric) at a given polarity. In this study we focus on the rising slope of the applied voltage, when the metal electrode is anode and the streamer propagates towards the cathode covered by a dielectric, as shown in Figure 2(b). The current density maxima at rising slope decrease from $1.4 \times 10^5 \text{ A/m}^2$ for 5 kHz to almost a half at 100 kHz. As the current density decreases for the rising slope for higher frequencies, one can see also the smaller and longer current density hump for the discharges at the falling slope.

The corresponding development of $|E|/N$ in the barrier discharges is shown in Figure 3(b). Here, only the important time interval of the half-period is selected, i.e. where the streamer manifests itself with an enhanced reduced electric field strength as it propagates towards the cathode and the electric field peaks at the dielectric surface vicinity. The maximum values of the corresponding E/N scales for each condition clearly show that the peak E/N decreases with increasing frequency. The reduced

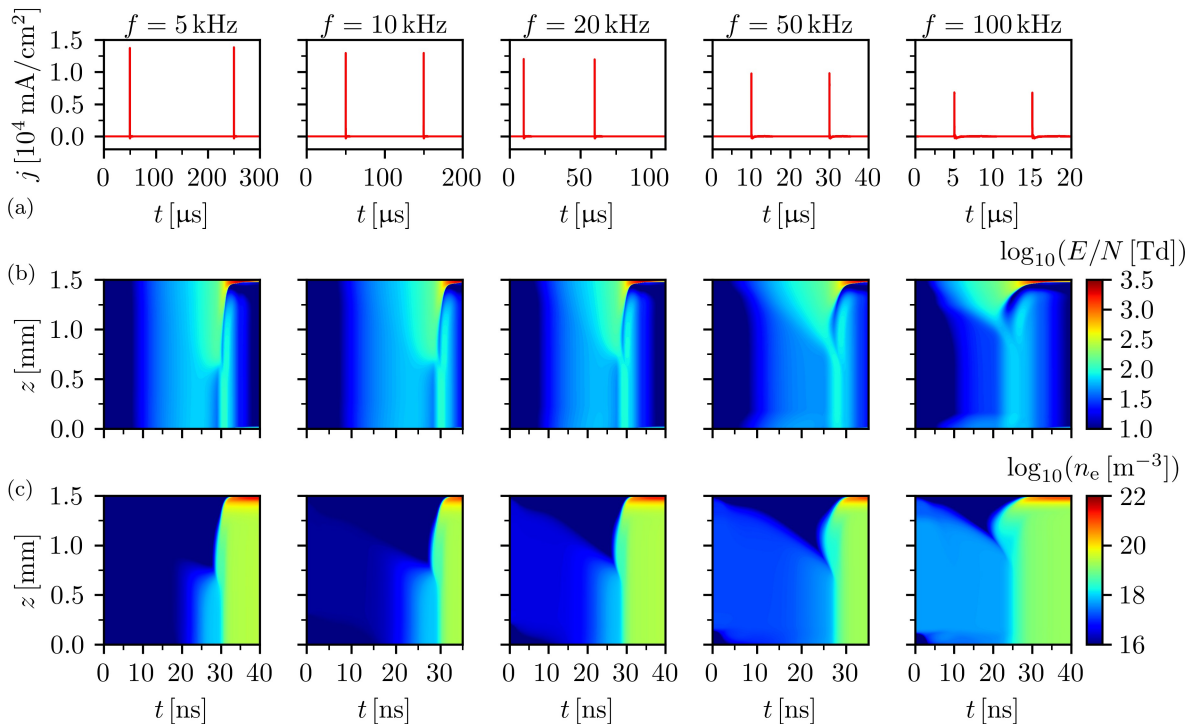


Figure 3. 1D modelling results for nanosecond pulsed discharges: (a) period evolution of the current density j as well as (b) magnitude $|E|/N$ of the reduced electric field and (c) electron density n_e during the streamer propagation and arrival to the dielectric surface for the same conditions. The cathode is placed under the dielectric surface as described earlier. Results for frequencies in the range from 5 to 100 kHz are presented. Note that the time after reaching quasi-periodic condition was subtracted in the figures.

electric field strength peaks as the streamer reaches the dielectric surface and for 5 kHz it is approx. 2300 Td. The peak value for the 100 kHz case is approx. 1840 Td. Corresponding results and maximum values of the electron density in the middle of the gap ($z = 0.75$ mm) and in the cathode region are summarized in Table 2.

From the local maxima of the E/N spatiotemporal distribution, the moving streamer head, one can determine the velocity of the propagating streamer v_{streamer} . Here, the mean velocity was determined from the time of the movement of the electric field maximum between two points near the cathode at 1.2 and 1.4 mm. The results are also given in Table 2. It is apparent that v_{streamer} decreases with increasing frequency.

The corresponding development of the electron number density for the relevant time intervals of the half-period of the discharges is presented in Figure 3(c) for the respective frequencies. Apparently, the higher the frequency the higher is the residual electron density in the gap which influences the initial ionization and the start of the streamer. The initial electron densities, describing the preionization before the discharge ignites, are given in Table 3. They range from approx. 10^{15} m^{-3} for 5 kHz to 10^{17} m^{-3} for

100 kHz. At the same time, it is apparent that the maximum electron density in the established transient discharge channel decreases with the increase of the frequency, which is a result of the lower electric field in the gap. The electron density in the discharge channel decreases from $3.1 \times 10^{19} \text{ m}^{-3}$ for 5 kHz to $1.92 \times 10^{19} \text{ m}^{-3}$ for 100 kHz. (cf. Table 2).

The above parameters of the investigated microdischarges are strongly influenced by the preceding discharges, i.e. the initial conditions at the beginning of each period in the periodic state. These initial conditions of interest are given by the number densities of electrons, metastables and other excited states (2p and 1s) in the gap. Their values for each frequency are given in Table 3. Such data serves as reference for further discussion of the applicability of the proposed diagnostic method using the densities of the 2p states.

The 2D modelling studies serve to investigate the effect of radial signal integration as it takes place during measurements. Barrier discharge filaments at atmospheric pressure usually show a diameter of tens to hundreds of microns and the possibilities to resolve the radial structure are therefore very limited, if not impossible (compare [42]). As the given fluid model is solved both in spatially 1D and 2D geometries, it is

Table 2. Maxima of the electron number density and reduced electric field in the middle of the gap ($z = 0.75$ mm) and in the cathode region (CR) for first and quasi-periodic discharge. The last row displays the streamer velocity determined from the movement of the electric field maximum between $z = 1.2$ mm and $z = 1.4$ mm during streamer propagation.

Quantity	1 st disch.	5 kHz	10 kHz	20 kHz	50 kHz	100 kHz
$n_e(0.75 \text{ mm}) [10^{19} \text{ m}^{-3}]$	3.65	3.10	2.30	2.87	1.87	1.92
$E/N(0.75 \text{ mm}) [\text{Td}]$	168	121	103	86	82	68
$n_e(\text{CR}) [10^{21} \text{ m}^{-3}]$	3.87	2.33	1.10	1.85	1.05	0.84
$E/N(\text{CR}) [\text{Td}]$	2702	2297	2241	2192	2065	1842
$v_{\text{streamer}} [10^6 \text{ m/s}]$	0.28	0.21	0.18	0.15	0.07	0.05

Table 3. Initial number densities of electrons and excited atomic argon species at the beginning of the period (i.e. $t = T$) in m^{-3} for different repetition frequencies (for first and quasi-periodic discharge) averaged between $z = 0.5$ and $z = 1$ mm, far from the sheath regions.

Species	1 st disch.	5 kHz	10 kHz	20 kHz	50 kHz	100 kHz
e	2×10^9	6.59×10^{15}	1.45×10^{16}	3.46×10^{16}	1.47×10^{17}	4.73×10^{17}
Ar[1s ₅]	10^9	1.98×10^{12}	9.05×10^{12}	5.16×10^{13}	7.61×10^{14}	5.38×10^{15}
Ar[1s ₄]	10^9	1.81×10^{13}	8.29×10^{13}	4.70×10^{14}	6.61×10^{15}	4.17×10^{16}
Ar[1s ₃]	10^9	3.19×10^{12}	1.45×10^{13}	8.13×10^{13}	1.12×10^{15}	7.00×10^{15}
Ar[1s ₂]	10^9	3.44×10^{12}	1.56×10^{13}	8.75×10^{13}	1.19×10^{15}	7.56×10^{15}
Ar[2p ₁₀]	10^9	1.94×10^9	8.78×10^9	4.88×10^{10}	6.57×10^{11}	3.98×10^{12}
Ar[2p ₉]	10^9	1.57×10^9	7.10×10^9	3.94×10^{10}	5.32×10^{11}	3.22×10^{12}
Ar[2p ₈]	10^9	2.08×10^9	9.42×10^9	5.23×10^{10}	7.05×10^{11}	4.27×10^{12}
Ar[2p ₇]	10^9	7.51×10^8	3.40×10^9	1.89×10^{10}	2.54×10^{11}	1.54×10^{12}
Ar[2p ₆]	10^9	5.68×10^9	2.57×10^{10}	1.43×10^{11}	1.93×10^{12}	1.16×10^{13}
Ar[2p ₅]	10^9	1.30×10^9	5.89×10^9	3.27×10^{10}	4.41×10^{11}	2.67×10^{12}
Ar[2p ₄]	10^9	7.86×10^8	3.55×10^9	1.97×10^{10}	2.66×10^{11}	1.61×10^{12}
Ar[2p ₃]	10^9	4.41×10^8	1.99×10^9	1.11×10^{10}	1.49×10^{11}	9.03×10^{11}
Ar[2p ₂]	10^9	5.59×10^8	2.53×10^9	1.41×10^{10}	1.89×10^{11}	1.15×10^{12}
Ar[2p ₁]	10^9	1.72×10^9	7.80×10^9	4.33×10^{10}	5.84×10^{11}	3.53×10^{12}

important to point out some differences in their results, which are caused by neglecting radial effects in the 1D model. The comparison of the first discharge (single shot) simulation using the 2D and the 1D model is shown in Figure 4. Both cases show a gradual increase of the electron density with increasing applied voltage, leading to the accumulation of space charges near the temporary anode. The accumulated space charge leads to the inception of the positive streamer near $z \approx 0.25$ mm around $t = 37$ ns in the 2D model and 36.5 ns in the 1D model. As the streamer propagates towards the cathode, $|E|/N$ and the electron number density start to increase. Note that they increase more gradually in the 1D model due to the neglect of the radial constriction of the channel, which results in lower $|E|/N$ in comparison to the 2D model. This is reflected by a much more rapid increase to the maximum in the 2D model in comparison to the 1D model. At the same time, the acceleration of the streamer towards the dielectric-covered cathode is well

visible in both cases and is stopped first directly in the vicinity of the dielectric surface. This is in agreement with the experimental data on streamers in pulsed or sinusoidal barrier discharges in argon [22, 43]. Note that in contrast to the 1D results, where the streamer slows down much earlier (around $t = 39.7$ ns) and farther away from the cathode (hundreds of microns), in 2D model it approaches the cathode to a few tens of microns around $t = 40.6$ ns resulting in a stronger $|E|/N$. However, the electron number density in the 1D model keeps increasing over time in the cathode region, eventually reaching a similar order of magnitude as in the 2D model (cf. Table 2).

It is important to note that the primary objective of this work is not to determine the electric field as accurately as possible or to validate the accuracy of the models against the experiment. Rather, the aim is to employ the modelling results to evaluate the line intensity ratio method for argon and find the most suitable combination of states for electric field

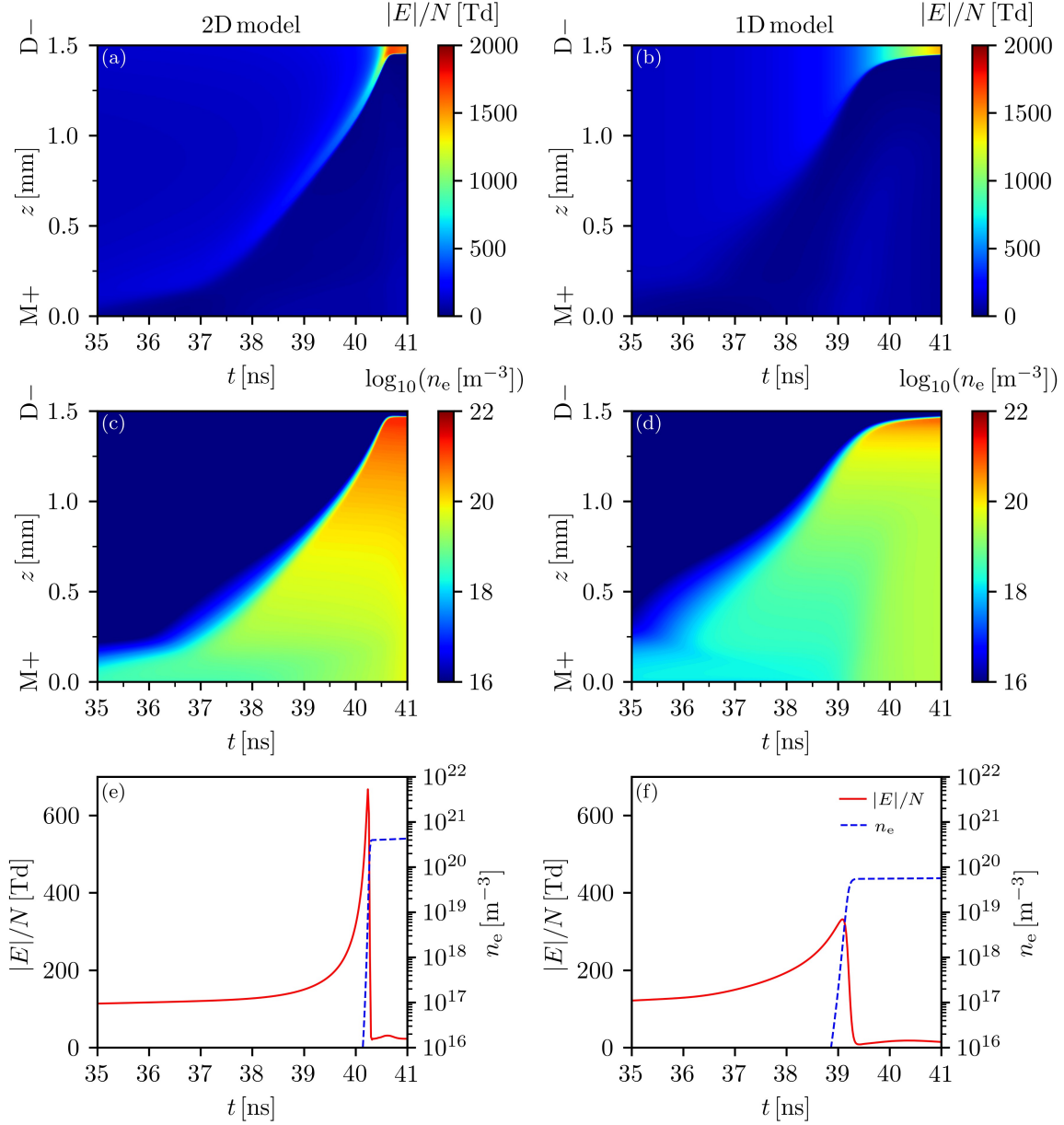


Figure 4. The magnitude of the reduced electric field and electron number density obtained by (a) and (c) 2D and (b) and (d) 1D model calculations. The development of these quantities is also highlighted for the position 1.24 mm in (e) and (f).

determination, in general. Since both the 1D and the 2D fluid-Poisson model self-consistently couple the electric field with the species densities, this can be achieved by using the computationally more efficient 1D model.

As mentioned earlier, semi-automated evaluation of a large amount of complex model calculations is time consuming and we are therefore limited here to the 1D

modelling results. Within all 1D and 2D simulations, the distributions of densities of all other species were obtained, too. Such data are analysed later in the text together with the effect of density (signal intensity in experiment) integration on the intensity ratio for E/N determination.

3.2. Investigation of 2p states suitable for the intensity ratio method

The intensity ratio method originates from the simplification of the full reaction kinetics model (RKM, as described by the equation (1)) to a very few processes which dominate the populations of the investigated radiative states, the so called simple CRM. For the case of air, as shown in Obrušník *et al.* [29], these processes are the direct electron impact excitation from the ground state as the only gain processes, the spontaneous emission, given by the radiative lifetime, and the collisional quenching by collisions with neutral gas. Here for the case of argon plasma, due to the presence of argon metastable states and other processes as denoted in the equation (1), such simplification is expected to be problematic. We have approached this issue in the following way: all processes (except the direct electron impact excitation from the ground state of argon) are lumped into an effective lifetime parameter, which is potentially time- and space-dependent (as basically all the source-term processes given in the equation (1) are). We then investigate the possible quantification of this effective lifetime parameter of a given 2p state best suitable for experimental use. With this, the balance equation reads

$$\frac{dn_{2p_i}(z,t)}{dt} = n_e(z,t) \cdot n_g \cdot k_{g,2p_i}(E(z,t)/N) - \frac{n_{2p_i}(z,t)}{\tau_{\text{eff}}^{2p_i}(z,t)}, \quad (3)$$

where z describes the axial coordinate in the gas gap and $\tau_{\text{eff}}^{2p_i}$ denotes the respective effective lifetime. We assume the ground state concentration to be constant in the gap. To derive an equation for the intensity (in our case the density) ratio method we select two 2p states i and j and divide their balance equations yielding the relation

$$\frac{dn_{2p_i}(z,t)/dt + n_{2p_i}(z,t)/\tau_{\text{eff}}^{2p_i}(z,t)}{dn_{2p_j}(z,t)/dt + n_{2p_j}(z,t)/\tau_{\text{eff}}^{2p_j}(z,t)} = \frac{k_{g,2p_i}(E(z,t)/N)}{k_{g,2p_j}(E(z,t)/N)} \quad (4)$$

Having the spatiotemporal development of the 2p state densities from the 1D model simulations, we rely only on the rate coefficient ratio for the selected pair of 2p states and on the variable $\tau_{\text{eff}}^{2p_i}(z,t)$. The rate coefficients for electron collision processes were obtained by solving the electron Boltzmann equation in multi-term approximation [44] using the cross-section set from [45, 46] as presented in [1]. The rate coefficients and their selected ratios are presented in Figure 5. Dominantly, the ratios including the rate coefficients for direct excitation of the 2p₂, 2p₃ and 2p₄ states are discussed here, see [22] and text below. The proper determination of the effective lifetimes $\tau_{\text{eff}}^{2p_i}(z,t)$ is more challenging and requires certain assumptions. As all the processes determining the effective lifetimes are included in the fluid-Poisson

model, we selected the following three ways for their quantification considering that a quantification or use of the lifetimes from or for measured data is the ultimate goal.

First, we include only all loss processes $S_{2p_i, \text{all losses}}(z,t)$ in the $\tau_{\text{eff}}^{2p_i}(z,t)$ for given 2p_{*i*} and denote it as type 1 effective lifetime $\tau_{\text{eff},1}^{2p_i}(z,t)$ defined as

$$\tau_{\text{eff},1}^{2p_i}(z,t) = \frac{1}{S_{2p_i, \text{all losses}}(z,t)}. \quad (5)$$

Such choice has its importance and applicability in the relative spatiotemporal stability of this lifetime and give us an almost constant number without large spatiotemporal variations. This was evaluated from the 1D simulations of the repetitive nanosecond pulsed barrier discharge under consideration and is shown in Figure 6(a) for the spatial coordinate of $z = 1.24$ mm at 10 kHz frequency of the pulse repetition. The temporal stability of the $\tau_{\text{eff},1}^{2p_i}(t)$ during the electric field rise time is apparent.

Second, we include all processes $S_{2p_i}(z,t)$ contributing to the population and depopulation of the 2p_{*i*} state density, except the direct electron impact driven process given by the rate $k_{g,2p_i}(E(z,t)/N)$. The latter is given separately in the balance equation. This should be the best option, as it describes the state density with the accuracy of equation (1). For experimental uses, such parameter is basically inaccessible due to its rapid temporal variation. We denote it as type 2 effective lifetime $\tau_{\text{eff},2}^{2p_i}(z,t)$ given by

$$\tau_{\text{eff},2}^{2p_i}(z,t) = \frac{1}{S_{2p_i}(z,t) - k_{g,2p_i}(E(z,t)/N) \cdot n_e(z,t) \cdot n_g}. \quad (6)$$

The results for the same conditions as for the type 1 lifetime are shown in Figure 6(b). The type 2 lifetimes are negative in most of their temporal range because the excitation rates are larger than the other loss processes in $S_{2p_i}(z,t)$ and result in sharp peaks where direct excitation to the 2p_{*i*} state dominates the source term S_{2p_i} (and the definition (6) becomes problematic due to division by zero). Due to these complex properties, the $\tau_{\text{eff},2}^{2p_i}(z,t)$ is not used in the presented evaluations and its more detailed analysis is left for future work.

In a third approach, we quantify the effective lifetimes of type 3, $\tau_{\text{eff},3}^{2p_i}(z,t)$, from the exponential decay of the 2p state densities after the streamer head passage. This is the only experimentally accessible effective lifetime. It can be measured with a detector of a sufficient, typically sub-nanosecond, temporal resolution, i.e. streak camera, fast photomultiplier, fast gated intensified CCD camera or a time-correlated single photon counting technique. Effective lifetimes and quenching coefficients were experimentally determined by this method already previously, see for example [47–49]. This evaluation procedure is illustrated

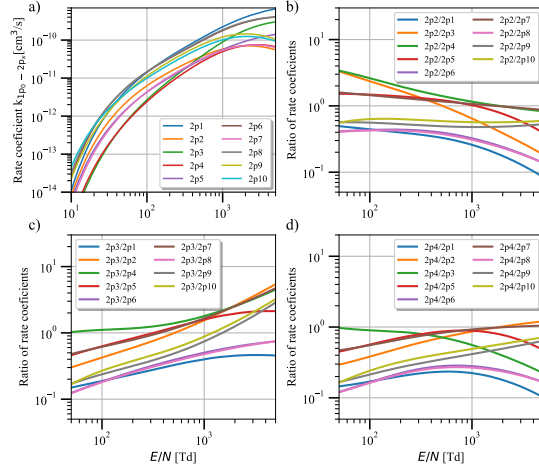


Figure 5. Rate coefficients of $2p_{1-10}$ argon states (a) and ratios of rate coefficients with upper state $2p_2$ (b), $2p_3$ (c) and $2p_4$ (d) as a function of E/N .

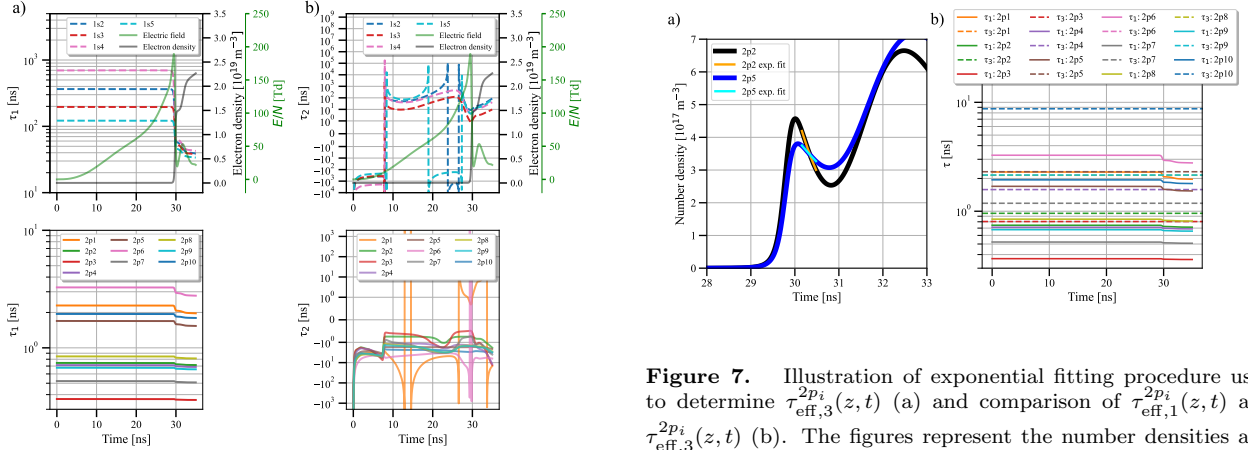


Figure 6. Temporal development of $\tau_{\text{eff},1}(z,t)$, (a), and $\tau_{\text{eff},2}(z,t)$, (b), during the quasi-periodic discharge as obtained from 1D simulations. The first row corresponds to the effective lifetimes of $1s_{2-5}$ states compared with the E/N and electron number density waveforms. The second row depicts effective lifetimes of $2p_{1-10}$ states. The effective lifetimes are shown for a discharge frequency of 10 kHz and spatial coordinate of 1.24 mm. Note that in figures (b) the interval -1 : 1 is linear for better data presentation.

together with its results in Figure 7 for the investigated discharge and compared to the effective lifetime of type 1 according to 5. The determined values of $\tau_{\text{eff},1}^{2p_i}(z,t)$ and $\tau_{\text{eff},3}^{2p_i}(z,t)$ are also given in Table 4. It should be noted that in some cases the decay of the $2p$ state densities after the streamer head was overlapped with the later discharge phase, making the determination of $\tau_{\text{eff},3}^{2p_i}(z,t)$ impossible. These values are missing in Table 4 and Figure 7. The overlap problem is also the reason for the failure of this effective lifetime determination in the real experiments, see further in the text.

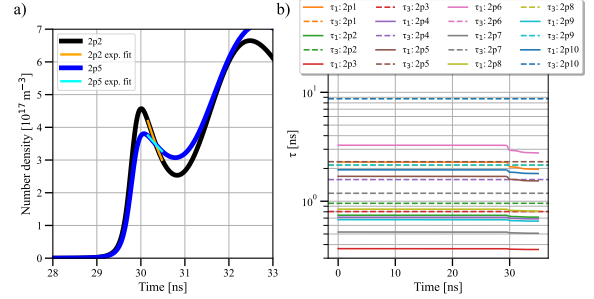


Figure 7. Illustration of exponential fitting procedure used to determine $\tau_{\text{eff},3}^{2p_i}(z,t)$ (a) and comparison of $\tau_{\text{eff},1}^{2p_i}(z,t)$ and $\tau_{\text{eff},3}^{2p_i}(z,t)$ (b). The figures represent the number densities and effective lifetimes for a discharge frequency of 10 kHz and spatial coordinate of $z = 1.24$ mm. Precise values of $\tau_{\text{eff},1}^{2p_i}(z,t)$ and $\tau_{\text{eff},3}^{2p_i}(z,t)$ are summarized in Table 4.

Having direct access to the defined effective lifetimes, we have performed a semi-automated evaluation of equation (4) using these lifetimes and used the $2p$ states densities obtained from the 1D simulations (point data) as well. The $2p$ state densities were available for different frequencies and coordinates in the gap for the nanosecond pulsed barrier discharge. An example of such evaluation for the 10 kHz repetitive discharge and the spatial coordinate of $z = 1.24$ mm is shown in Figure 8, where the first type of effective lifetime $\tau_{\text{eff},1}^{2p_i}(z,t)$ is used to evaluate the ratio of state densities $2p_2/2p_5$.

In Figure 8(a), the temporal developments of the densities of radiative states $2p_2$ and $2p_5$ (divided by the respective effective lifetimes $\tau_{\text{eff},1}^{2p_2}(z,t)$ and $\tau_{\text{eff},1}^{2p_5}(z,t)$) are shown, together with their derivatives and sums of these two components (total), for the coordinate of

Table 4. Effective lifetimes $\tau_{\text{eff},1}^{2P_i}(z, t)$ and $\tau_{\text{eff},3}^{2P_i}(z, t)$ for a discharge frequency of 10 kHz. The values for spatial coordinate 1.24 mm are also depicted in Figure 7(b). The values that could not be determined because of the streamer decay overlapping with subsequent discharge phases are not presented, including the entire spatial position of 1.48 mm. The spatial positions of the used $\tau_{\text{eff},1}^{2P_i}(z, t)$ are not specified as the values for individual positions are identical before the discharge.

Lifetime [ns]	2p ₁	2p ₂	2p ₃	2p ₄	2p ₅	2p ₆	2p ₇	2p ₈	2p ₉	2p ₁₀
τ_1	2.29	0.74	0.37	0.71	1.69	3.27	0.52	0.84	0.67	1.94
τ_3 (1 mm)	-	1.95	1.37	2.7	9.8	-	2.97	8.67	8.16	-
τ_3 (1.24 mm)	-	0.96	0.80	1.58	2.31	-	1.18	2.14	2.15	8.72

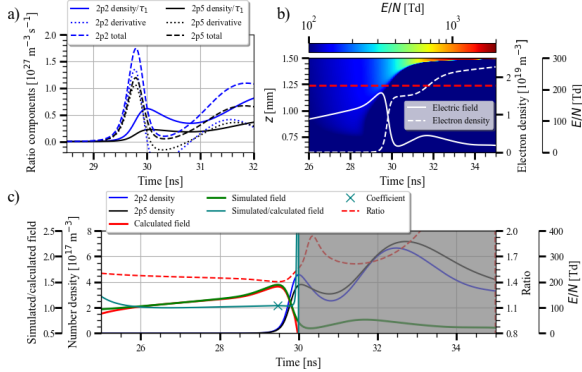


Figure 8. Determination of E/N and E/N multiplication coefficient from the ratio of 2p₂ to 2p₅ states from the 1D model. Figure (a) shows the temporal development of the components used for determination of E/N . Figure (b) displays the spatiotemporal behaviour of E/N from the 1D model for 10 kHz together with the profile of the E/N and electron number density at 1.24 mm. The spatial position 1.24 mm is depicted as the red dashed line and all of the displayed data in figure (a) and (c) corresponds to this position. In figure (c) the ratio of simulated to calculated field is denoted as a teal waveform, where the ratio of their maxima (E/N multiplication coefficient) is denoted as a teal cross. The red dashed line represents the ratio of total components in figure (a), i.e. the left side of equation (4). The shaded area in (c) corresponds to the discharge phase where direct electron impact excitation is not dominant (after the streamer head passed the spatial point) and therefore the presented method is not applicable, i.e. the range is out of interest for further analysis.

$z = 1.24$ mm. The coordinate is highlighted by the red dashed line in Figure 8(b) for better orientation. As also shown in [2], the density derivatives can be a dominant part of the left-hand side of equation (4). As it is obvious from Figure 8(a), they completely dominate at the very beginning. It is obvious, as we have a rapidly changing electric field in the passing fast streamer induced by the nanosecond pulse of applied voltage.

In Figure 8(c), the original simulated electric field from the fluid model simulation is shown (green) together with the electric field calculated from the equation (4) (red), using the selected effective lifetimes and the excitation rate coefficients as described earlier in the text. The ratio of simulated to calculated

E/N peak values is evaluated as so-called E/N multiplication coefficient, which further serves for quantification of the accuracy using equation (4) with given state densities and effective lifetimes for E/N determination. Obviously, the closer the multiplication coefficient is to unity, the better equation (4) approximates the complex generation and loss processes for the respective 2p state in the discharge under given conditions. As it was previously discussed, the presented intensity ratio method requires direct electron impact excitation from the ground state to be a dominant population process for the considered 2p states (all other processes are considered in an effective lifetime, see equation 1). However, this assumption is not valid after the streamer head has passed (approx. at 30 ns) because then stepwise excitation and quenching processes start to contribute significantly to the population of all 2p states. In this temporal region, marked as a shaded region in Fig.8(c), the calculated E/N represents an artefact and should not be considered for further analysis. More discussion regarding this artefact and its identification can be found for example in [2, 14, 50].

We have determined the multiplication coefficient for E/N during the streamer propagation phase in the nanosecond barrier discharge using a semi-automated procedure at different frequencies and for three spatial coordinates. The results are shown in Figure 9. Here we want to find the best suitable 2p states ratio by a “computational force” of simulating the discharge and evaluating the E/N using the equation (4) for different conditions and scenarios. This procedure has the following reasons. The different frequencies represent the different preionization and initial metastable state densities in the gas gap where the streamer propagates, as it was quantified earlier in subsection 3.1. The interval of their values is given by at least 2×10^9 (initial conditions for the first discharge) and at most $4.73 \times 10^{17} \text{ m}^{-3}$ (initial conditions for the 100 kHz discharge) for electron density and 10^9 m^{-3} at least and 10^{15} m^{-3} at most for the metastable states densities in the evaluated coordinates. The different coordinates of the E/N evaluation for all these frequencies then give the sensitivity of the searched 2p states ratio to the

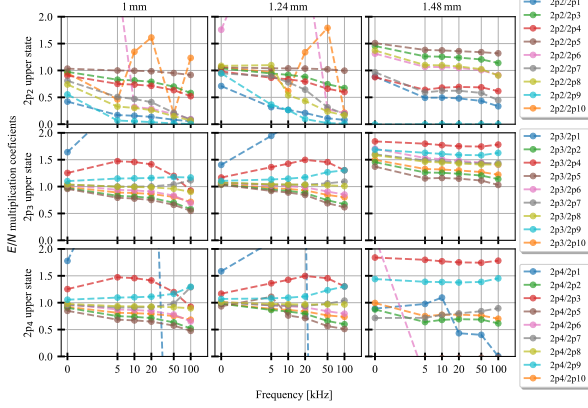


Figure 9. E/N multiplication coefficients with the application of $\tau_{\text{eff},1}^{2p_i}(z,t)$. The coefficients are displayed for all combinations of $2p_{1-10}$ states with $2p_2$, $2p_3$, and $2p_4$ upper states, they are displayed as individual rows. The columns represent spatial positions 1, 1.24, and 1.48 mm. Calculations are conducted based on results of 1D simulations for frequencies of 5, 10, 20, 50 and 100 kHz and also for the first discharge depicted as 0 kHz. The frequencies are displayed in logarithmic scale with the interval from 0 to 5 kHz being linear.

electric field of different amplitudes. The evaluated interval of the amplitudes is from 100 to 2200 Td, approximately.

The semi-automated procedure consists of following phases: The first phase of the semi-automated procedure is the determination of the E/N based on equation (4) by the use of $\tau_{\text{eff}}^{2p_i}(z,t)$ (type 1 and 3), see Figure 7, and the use of number densities of respective $2p$ states. The individual components of this evaluation can be seen in Figure 8 with the resulting ratio of the left-hand side of equation (4) in Figure 8(c) depicted as a red dashed line. The determination of E/N from the density ratios is based on the rate coefficients shown in Figure 5.

The second phase of the procedure is concerned with the evaluation of the E/N multiplication coefficient, i.e. the ratio of peak values of the simulated and the calculated electric field. The procedure is however not as straightforward for the calculated fields as their temporal profile often displays local variations that tend to disrupt the process. One of the main reasons for these deviations is the low sensitivity of ratios of rate coefficients to E/N . This often leads to ambiguously defined E/N that fluctuate between multiple values. This is mostly countered by using extrapolated values of the ratio of rate coefficients for a selected range of E/N , typically 100 to 1000 Td (up to 2000 Td), see Figure 5. This is important information also for the possible experimental use of the intensity ratio. Above some E/N values the function of rate coefficients ratio changes the polarity

of its derivative and is not ambiguous with respect to the E/N . Another aspect to consider is the complexity of the temporal development of the calculated E/N . In the temporal range with low number densities of $2p$ states, the calculated E/N is often not very precise and significant fluctuations take place. Similar deviations are also present after the maximum of the streamer head where the CRM of the line ratio method using equation (4) is no longer valid. Such problems are also present in the evaluation of experimental data, see e.g. [2].

To suppress any persistent deviations of calculated E/N , only the very close proximity of the maximum of the simulated field is used to find the maximum of the calculated field to compare with. The calculated E/N in this temporal range is Gaussian smoothed and its time derivative is tracked. The maximum is marked when the derivative is equal to zero. It should be noted that the evaluation parameters (especially the temporal ranges tracked by time derivative) were set manually for every spatial position to increase the precision of the procedure. Even after all the corrections described above, the influence of the low sensitivity of ratios of rate coefficients on E/N and complex temporal development of the calculated E/N was still not completely suppressed. However, after a detailed investigation, it was concluded that only a few ambiguously defined E/N are present and mostly for the combinations among states $2p_{1,6-10}$. These problematic coefficients usually manifest themselves by their oscillatory nature as functions of frequency (see e.g. the coefficients for $2p_2/2p_{10}$ for position 1.24 mm in the centred part of the first row of Figure 9). The oscillatory behaviour also takes place for the ratio of states whose calculated E/N is significantly higher or lower than that of the simulated field. Those are typically the states in combination with $2p_1$.

By careful analysis of the results, we have found that using effective lifetimes of the first type, $\tau_{\text{eff},1}^{2p_i}(z,t)$, the coefficient is closer to unity for most frequencies and positions dominantly for the ratios including the states $2p_2$, $2p_3$ and $2p_4$. It was already previously estimated that these states should be dominantly populated by the direct electron impact excitation from the ground state using optical emission spectroscopy for the same nanosecond barrier discharge in argon, see [22]. Moreover, the ratio of $2p_2$ to $2p_5$ was found to be relatively stable for all three positions and over the investigated interval of pulse repetition frequencies. Ratios using the densities of $2p_8$ state in combination with $2p_3$ and $2p_4$ resulted also in an E/N multiplication coefficient close to unity. Thus, they might also become interesting for the use of the intensity ratio method and will be analysed in more detail in future studies.

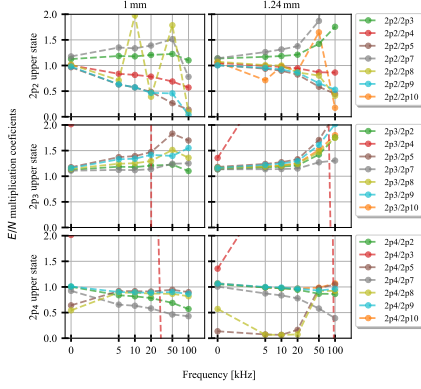


Figure 10. E/N multiplication coefficients with the application of $\tau_{\text{eff},3}^{2p_i}(z,t)$. The coefficients are displayed for all combinations of $2p_{1-10}$ states with $2p_2$, $2p_3$, and $2p_4$ upper states, they are displayed as individual rows. The columns represent spatial positions 1 and 1.24 mm. Calculations are conducted for 1D model at frequencies 5, 10, 20, 50 and 100 kHz and also for a first discharge depicted as 0 kHz. Note that coefficients for position 1.48 mm, ratio of states including $2p_1$, $2p_6$ and partly $2p_{10}$ are not displayed as their respective $\tau_{\text{eff},3}^{2p_i}(z,t)$ could not be determined, see table 4. The frequencies are displayed on a logarithmic scale with the interval from 0 to 5 kHz being linear.

Evaluating the E/N multiplication coefficients also for the third type of the effective lifetimes, i.e. $\tau_{\text{eff},3}^{2p_i}(z,t)$, we came to very similar results, see Figure 10. The figure shows the coefficients for all combinations of states with the upper states $2p_2$, $2p_3$ and $2p_4$ for positions 1 and 1.24 mm. The ratios containing the states $2p_1$, $2p_6$ and partly $2p_{10}$ are excluded from the evaluation, as it was not possible to determine positive values of their effective lifetimes, as shown in the table 4. However, based on the relatively good match of E/N multiplication coefficients for the remaining theoretical lifetimes of the type 3, we can state that also this approach can deliver reasonable E/N values. The ratio of $2p_4$ to $2p_9$ results in a good E/N computation over all frequencies and both positions.

3.3. Comparison with experimental data and effect of spatial integration of radiative state densities

The relatively robust ratio of $2p_2$ to $2p_5$ was used for evaluation of the experimental data presented in [22]. The same procedure for the determination of E/N , as shown in Figure 8, is conducted on measured number densities using the equation (4) and both proposed lifetimes. The resulting E/N compared with the E/N obtained from the 1D simulation is shown in Figure 11 together with the individual components on left hand side of equation (4). This figure also compares the influence of theoretically obtained effective lifetimes

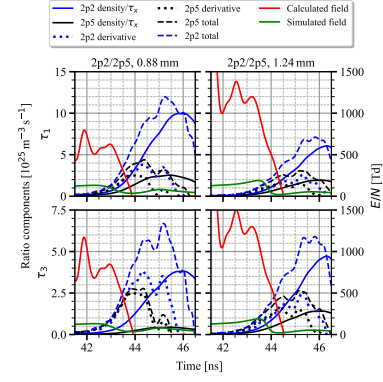


Figure 11. Smoothed components necessary for intensity ratio technique, see equation (4), with resulting E/N . The figure shows the results from an evaluation of ratio $2p_2/2p_5$ at two spatial positions 0.88 and 1.24 mm. Calculations were conducted on measured data discussed in detail in [22] with application of $\tau_{\text{eff},1}^{2p_i}(z,t)$ and $\tau_{\text{eff},3}^{2p_i}(z,t)$. The rows represent calculations with respective effective lifetimes, while the columns represent individual spatial coordinates. The simulated (green) E/N is not temporally correlated with the calculated field and is only used for a comparison of fields maxima, not temporal position.

of type 1 and 3 on computed E/N , with fairly similar results of difference ~ 200 Td for 0.88 mm (experimental position 0.88 mm was compared with the simulated position of 1 mm) and ~ 100 Td for 1.24 mm. It is important to mention that the relevant value of E/N in the streamer head is located in the proximity of 43 ns. Notice that similarly as in the case of simulated data, the time derivatives of the densities of $2p$ states are an important contribution to the total quantity (i.e. to numerator or denominator of the equation (4)). Probably due to the limited temporal resolution or lower signal-to-noise ratio in the measurements, the derivatives are not as dominant as in the case of simulated data. As the values of $2p$ states' number densities are in that moments relatively low, they are prone to fluctuations and subsequently so are the derivatives. Nevertheless, despite the fluctuations of the derivatives and the low sensitivity of E/N on the ratio of rate coefficients, the proposed ratio $2p_2/2p_5$ is in qualitative agreement with the simulated field for the two positions. Figure 11 also indicates that the E/N increases for coordinates closer to the cathode, as expected, showing that even in experimental conditions the determination of E/N by the intensity ratio method is possible, i.e. sensitive to E/N variations. This suggests that the ratio $2p_2/2p_5$ may be one of the best options found for E/N determination by a presented method, even if the absolute values are unphysically high.

An important aspect that should be considered is that the optical emission spectroscopy measurement is a line-of-sight integration detection. As mentioned

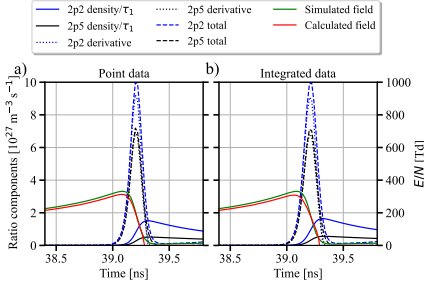


Figure 12. Comparison of ratio components of point data and their integrated values over an axial interval of $30 \mu\text{m}$ for first discharge and position of 1.24 mm . Data are from a 1D simulation. The integrated data are in $\text{m}^{-2}\text{s}^{-1}$ and are scaled by the ratio of the maxima of $2p_2$ totals for illustrative purposes. The simulated field (green curves) corresponds to the E/N of point data for both parts of the graph.

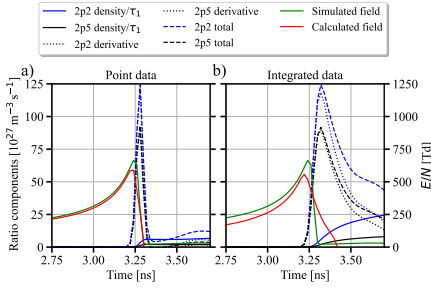


Figure 13. Comparison of ratio components of point data and their integrated values over a volume interval of $30 \mu\text{m}$ for first discharge and position of 1.24 mm . Data are from a 2D simulation. The integrated data are in s^{-1} and are scaled by the ratio of the maxima of $2p_2$ totals for illustrative purposes. The simulated field (green curves) corresponds to the E/N of point data for both parts of the graph.

previously, due to its microscopic diameter, the discharge filament is projected perpendicularly onto the monochromator slit. As a result, the measured intensities/densities are axially and radially integrated. To resolve this issue, the data obtained by using 1D and 2D model calculations are analysed in the further part of the manuscript.

The so far discussed point data ($2 \mu\text{m}$ cell on axis) of number densities are presented and compared with E/N computations from axially integrated (for 1D model, see Figure 12) and with volume integrated number densities (see Figure 13 for 2D model) for the first discharge at the position of 1.24 mm . The volume integration is given by equation (2). Both figures depict the individual ratio components, their calculated E/N (with an effective lifetime of type 1), and the simulated field.

In Figure 12, the comparison between point data and axially integrated data over $30 \mu\text{m}$ is shown. It shows that if the 1D simulated number densities are integrated in the axial dimension, the respective

calculated E/N is almost identical to the simulated E/N with deviation in units of Td for 1 and 1.24 mm for the selected ratio $2p_2/2p_5$. The values of the calculated field for point data in Figure 12 is 313 Td and the value for integrated data is 308 Td ; in comparison the value of the simulated field is 331 Td . Therefore, the deviation of the calculated fields from the simulated field is 18.6 Td for point data densities and 23.5 Td for integrated data densities. The significant difference occurs only for the case of 1.48 mm , presumably because it is only 0.02 mm from the electrode and the integration includes an area corresponding to the cathode spot, i.e. an area with a high spatiotemporal gradient of E/N .

In Figure 13 the comparison of point data and volume integrated data is shown. We can see that the match of the calculated and simulated field is not as good for integrated data as for point data. The integration of the densities using equation (2) results in computed E/N with lower amplitude and broader waveform. However, the amplitude deviation is still only 16% . Also, the influence of time derivatives is not as influential in the case of integrated data as in the case of point data evaluation and is similar to experimental data evaluation, compare with Figure 11.

4. Summary and conclusions

We have investigated the possibility of using the ratio of the densities of the $2p$ states for reduced electric field strength (E/N) determination from the optical emission spectra for nanosecond pulsed barrier discharges in argon at atmospheric pressure. To find robust pairs of $2p$ states, we have used the combined methodology of performing a large number of model calculations in 1D and 2D geometry for different frequencies from 5 kHz to 100 kHz and evaluating the data at different spatial coordinates in the gap during streamer development using a semi-automated procedure. Such an approach enabled us to study the applicability of selected $2p$ states for the E/N determination, based on a comparison of the calculated values with the original E/N given by the 1D and 2D modelling results, respectively. The computations were done for different positions in the streamer development to assess the sensitivity of the investigated $2p$ state ratios for E/N to initial metastable densities (up to approx. $7 \times 10^{15} \text{ m}^{-3}$ at maximum), electron densities (up to approx. $5 \times 10^{17} \text{ m}^{-3}$ at maximum) and for a wide range of E/N values (70 to 2200 Td).

The presented work is a required and important step towards introducing the line intensity ratio method for experimental determination of the electric field in highly transient argon plasmas. This step consists of exploring the possibilities of the described

methodology by means of numerical simulations and semi-automated evaluation of large amounts of data. The main purpose is to determine the sensitivity of selected reaction kinetic processes regarding changes of the electric field and to find out which measurable 2p levels of argon (in Paschen notation) are suitable to re-calculate the electric field from measured emission profiles. This can obviously be done only on the basis of numerical simulations providing the spatiotemporal development of all relevant 2p states, reaction rate coefficients as well as the electric field.

Special attention was paid to identify appropriate effective lifetimes of selected 2p states, as these are an important part of the E/N determination. Two effective lifetime definitions were proposed, which are considered to be useful for the evaluation of measurements in the laboratory.

Few ratios of 2p states were identified as the most robust ones. The density ratio $2p_4/2p_9$ shows good results for both evaluated effective lifetimes and most of the positions and frequencies. The computed E/N values evaluated from the density ratio $2p_2/2p_3$ do not show the best agreement with the simulated E/N , yet its ratio of excitation rate coefficients manifests a relatively good sensitivity to E/N . The most promising 2p states' ratio is $2p_2/2p_5$. It even shows qualitative agreement if applied to measured data, even though its rate coefficients' ratio is not very sensitive to the E/N value. This is a very promising result, clearly surpassing the expectations and overcoming the challenging limitation of the intensity ratio methods in general as they are currently known [2].

The results of the semi-automated procedure, in the form of the established E/N multiplication coefficients, have shown that for frequencies higher than 20 kHz and the area at close vicinity of the dielectric on the cathode, the uncertainty of almost all 2p states' ratios rises and makes its use for E/N determination far more complicated if not completely uncertain. This is mostly due to the increasing influence of indirect gain and loss processes for the 2p states, such as stepwise excitation.

Furthermore, we investigated the effect of axial and radial integration of the simulated particle densities on the E/N values calculated by the line intensity ratio method. The uncertainty generally remains in a reasonable range below 20%. It was shown as well that the axial integration of the signal (if the method is used in the experiment) over a few tens of microns is not as crucial as the radial integration.

The performed studies and analyses show the potential of quantifying the 2p states' ratios for the direct use in plasma diagnostics when combined with modelling studies. They also serve for the validation of the fluid-Poisson modelling and the recently

developed reaction kinetics scheme on sub-nanosecond and microscopic scales by direct comparison with experimental data of comparable spatiotemporal resolution. Such spatiotemporal scales of combined theoretical and direct experimental investigations were up to now mostly inaccessible. Moreover, the semi-automated procedure can be understood as a first step towards fully automated evaluation of large simulation data not only for plasma diagnostics.

Acknowledgments

This research was funded by the Czech Science Foundation project no.21-16391S and by the Deutsche Forschungsgemeinschaft (DFG, German Research Foundation) Projects No. 407462159 and 466331904. This research has been also supported by the project LM2023039 funded by the Ministry of Education, Youth and Sports of the Czech Republic.

References

- [1] Stankov M, Becker M M, Hoder T and Loffhagen D 2022 *Plasma Sources Science and Technology* **31** 125002 URL <https://dx.doi.org/10.1088/1361-6595/ac9332>
- [2] Goldberg B M, Hoder T and Brandenburg R 2022 *Plasma Sources Science and Technology* **31** 073001 URL <https://dx.doi.org/10.1088/1361-6595/ac6e03>
- [3] Massines F, Sarra-Bournet C, Fanelli F, Naudé N and Gherardi N 2012 *Plasma Processes and Polymers* **9** 1041–1073 URL <https://doi.org/10.1002/ppap.201200029>
- [4] Adamovich I, Baalrud S D, Bogaerts A, Bruggeman P J, Cappelli M, Colombo V, Czarnetzki U, Ebert U, Eden J G, Favia P, Graves D B, Hamaguchi S, Hieftje G, Hori M, Kaganovich I D, Kortshagen U, Kushner M J, Mason N J, Mazouffre S, Thagard S M, Metelmann H R, Mizuno A, Moreau E, Murphy A B, Niemira B A, Oehrlein G S, Petrovic Z L, Pitchford L C, Pu Y K, Rauf S, Sakai O, Samukawa S, Starikovskaia S, Tennyson J, Terashima K, Turner M M, van de Sanden M C M and Vardelle A 2017 *Journal of Physics D: Applied Physics* **50** 323001 URL <https://doi.org/10.1088/1361-6463/aa76f5>
- [5] Desjardins E, Laurent M, Durocher-Jean A, Laroche G, Gherardi N, Naudé N and Stafford L 2018 *Plasma Sources Science and Technology* **27** 015015 URL <https://dx.doi.org/10.1088/1361-6595/aaa5d9>
- [6] Reuter S, von Woedtke T and Weltmann K D 2018 *Journal of Physics D: Applied Physics* **51** 233001 URL <https://doi.org/10.1088/1361-6463/aab3ad>
- [7] Loffhagen D, Becker M M, Hegemann D, Nisol B, Watson S, Wertheimer M R and Klages C P 2020 *Plasma Processes and Polymers* **17** 1900169 (Preprint <https://onlinelibrary.wiley.com/doi/pdf/10.1002/ppap.201900169>) URL <https://onlinelibrary.wiley.com/doi/abs/10.1002/ppap.201900169>
- [8] Czarnetzki U, Luggenhölscher D and Döbele H F 1998 *Phys. Rev. Lett.* **81**(21) 4592–4595 URL <https://link.aps.org/doi/10.1103/PhysRevLett.81.4592>
- [9] Barnat E V and Hebner G A 2004 *Applied Physics Letters* **85** 3393–3395 (Preprint <https://doi.org/10.1063/1.1766075>) URL <https://doi.org/10.1063/1.1766075>
- [10] Goldberg B M, Reuter S, Dogariu A and Miles R B 2019

- Opt. Lett.* **44** 3853–3856 URL <https://opg.optica.org/ol/abstract.cfm?URI=ol-44-15-3853>
- [11] Du B, Sadeghi N, Tsankov T V, Luggenhölscher D and Czarnetzki U 2012 *Plasma Sources Science and Technology* **21** 045015 URL <https://doi.org/10.1088/0963-0252/21/4/045015>
- [12] Siepa S, Danko S, Tsankov T V, Mussenbrock T and Czarnetzki U 2014 *Journal of Physics D: Applied Physics* **47** 445201 URL <https://doi.org/10.1088/0022-3727/47/44/445201>
- [13] Dyatko N A, Ionikh Y Z and Meshchanov A V 2021 *Plasma Sources Science and Technology* **30** 055015 URL <https://doi.org/10.1088/1361-6595/abda9e>
- [14] Kozlov K V, Wagner H E, Brandenburg R and Michel P 2001 *Journal of Physics D: Applied Physics* **34** 3164–3176 URL <https://doi.org/10.1088/0022-3727/34/21/309>
- [15] Bonaventura Z, Bourdon A, Celestin S and Pasko V P 2011 *Plasma Sources Science and Technology* **20** 035012 URL <https://dx.doi.org/10.1088/0963-0252/20/3/035012>
- [16] Hoder T, Šimek M, Bonaventura Z, Prukner V and Gordillo-Vázquez F J 2016 *Plasma Sources Science and Technology* **25** 045021 URL <https://dx.doi.org/10.1088/0963-0252/25/4/045021>
- [17] Jánský J, Bessières D, Brandenburg R, Paillol J and Hoder T 2021 *Plasma Sources Science and Technology* **30** 105008 URL <https://doi.org/10.1088/1361-6595/ac2043>
- [18] Hoder T, Höft H, Kettlitz M, Weltmann K D and Brandenburg R 2012 *Physics of Plasmas* **19** 070701 ISSN 1070-664X (Preprint https://pubs.aip.org/aip/pop/article-pdf/doi/10.1063/1.4736716/16112209/070701_1_online.pdf) URL <https://doi.org/10.1063/1.4736716>
- [19] Jiang W, Tang J, Wang Y, Zhao W and Duan Y 2013 *Physics of Plasmas* **20** 073509 ISSN 1070-664X (Preprint https://pubs.aip.org/aip/pop/article-pdf/doi/10.1063/1.4817289/16033451/073509_1_online.pdf) URL <https://doi.org/10.1063/1.4817289>
- [20] Magnan R, Hagelaar G, Chaker M and Massines F 2020 *Plasma Sources Science and Technology* **29** 035009 URL <https://dx.doi.org/10.1088/1361-6595/ab4cfe>
- [21] Bazinette R, Sadeghi N and Massines F 2020 *Plasma Sources Science and Technology* **29** 095010 URL <https://dx.doi.org/10.1088/1361-6595/ab8686>
- [22] Kusýn L, Prokop D, Navrátil Z and Hoder T 2023 *Plasma Sources Science and Technology* **32** 045006 URL <https://dx.doi.org/10.1088/1361-6595/acc6eb>
- [23] Malagón-Romero A, Pérez-Invernón F J, Luque A and Gordillo-Vázquez F J 2019 *Journal of Geophysical Research: Atmospheres* **124** 12356–12370 (Preprint <https://agupubs.onlinelibrary.wiley.com/doi/pdf/10.1029/2019JD030945>) URL <https://agupubs.onlinelibrary.wiley.com/doi/abs/10.1029/2019JD030945>
- [24] Heijkens S, Aghaei M and Bogaerts A 2020 *The Journal of Physical Chemistry C* **124** 7016–7030 URL <https://doi.org/10.1021/acs.jpcc.0c00082>
- [25] Zhu X M and Pu Y K 2010 *Journal of Physics D: Applied Physics* **43** 403001 URL <https://dx.doi.org/10.1088/0022-3727/43/40/403001>
- [26] Bílek P, Kuthanová L, Hoder T and Šimek M 2022 *Plasma Sources Science and Technology* **31** 084004 URL <https://dx.doi.org/10.1088/1361-6595/ac7ad1>
- [27] Jovanović A P, Hoder T, Höft H, Loffhagen D and Becker M M 2023 *Plasma Sources Science and Technology* **32** 055011 URL <https://dx.doi.org/10.1088/1361-6595/acd2fc>
- [28] Mrkvičková M, Kuthanová L, Bílek P, Obrusník A, Navrátil Z, Dvořák P, Adamovich I, Šimek M and Hoder T 2023 *Plasma Sources Science and Technology* **32** 065009 URL <https://dx.doi.org/10.1088/1361-6595/acd6de>
- [29] Obrusník A, Bílek P, Hoder T, Šimek M and Bonaventura Z 2018 *Plasma Sources Science and Technology* **27** 085013 URL <https://dx.doi.org/10.1088/1361-6595/aad663>
- [30] Paris P, Aints M, Valk F, Plank T, Haljaste A, Kozlov K V and Wagner H E 2005 *Journal of Physics D: Applied Physics* **38** 3894 URL <https://dx.doi.org/10.1088/0022-3727/38/21/010>
- [31] Bílek P, Obrusník A, Hoder T, Šimek M and Bonaventura Z 2018 *Plasma Sources Science and Technology* **27** 085012 URL <https://dx.doi.org/10.1088/1361-6595/aad666>
- [32] Bílek P, Šimek M and Bonaventura Z 2019 *Plasma Sources Science and Technology* **28** 115011 URL <https://dx.doi.org/10.1088/1361-6595/ab3936>
- [33] Jögi I, Levoll E, Paris P and Aints M 2016 Comparison of experimental and theoretical spectra of non-self-sustained discharge in nitrogen and air in wide range of field strength and pressure *Proc. 15th High Pressure Low Temperature Plasma Chemistry Symp.* (Masaryk University, Brno, Czech Republic) p 118 ISBN 978-80-210-8318-9
- [34] Brisset A, Gazeli K, Magne L, Pasquiers S, Jeanney P, Marode E and Tardiveau P 2019 *Plasma Sources Science and Technology* **28** 055016 URL <https://dx.doi.org/10.1088/1361-6595/ab1989>
- [35] Dijcks S, Kusýn L, Janssen J, Bílek P, Nijdam S and Hoder T 2023 *Frontiers in Physics* **11** ISSN 2296-424X URL <https://www.frontiersin.org/articles/10.3389/fphy.2023.1120284>
- [36] Jovanović A P, Stankov M N, Loffhagen D and Becker M M 2021 *IEEE Transactions on Plasma Science* **49** 3710–3718
- [37] Jovanović A P, Loffhagen D and Becker M M 2022 *Plasma Sources Science and Technology* **31** 04LT02 URL <https://dx.doi.org/10.1088/1361-6595/ac63df>
- [38] Hoder T, Loffhagen D, Wilke C, Grosch H, Schäfer J, Weltmann K D and Brandenburg R 2011 *Phys. Rev. E* **84**(4) 046404 URL <https://link.aps.org/doi/10.1103/PhysRevE.84.046404>
- [39] Becker M M, Hoder T, Brandenburg R and Loffhagen D 2013 *Journal of Physics D: Applied Physics* **46** 355203 URL <https://doi.org/10.1088/0022-3727/46/35/355203>
- [40] Šimek M, Ambrico P F, Hoder T, Prukner V, Dilecce G, Benedictis S D and Babický V 2018 *Plasma Sources Science and Technology* **27** 055019 URL <https://dx.doi.org/10.1088/1361-6595/aac240>
- [41] Höft H, Kettlitz M, Becker M M and Brandenburg R 2019 *Journal of Physics D: Applied Physics* **53** 025203 URL <https://dx.doi.org/10.1088/1361-6463/ab4944>
- [42] Šimek M and Ambrico P F 2012 *Plasma Sources Science and Technology* **21** 055014 URL <https://dx.doi.org/10.1088/0963-0252/21/5/055014>
- [43] Kloc P, Wagner H E, Trunec D, Navrátil Z and Fedoseev G 2010 *Journal of Physics D: Applied Physics* **43** 345205 URL <https://dx.doi.org/10.1088/0022-3727/43/34/345205>
- [44] Leyh H, Loffhagen D and Winkler R 1998 *Computer Physics Communications* **113** 33–48 ISSN 0010-4655 URL <https://www.sciencedirect.com/science/article/pii/S0010465598000629>
- [45] Zatsarinny O, Wang Y and Bartschat K 2014 *Phys. Rev. A* **89**(2) 022706 URL <https://link.aps.org/doi/10.1103/PhysRevA.89.022706>
- [46] Zatsarinny O and Bartschat K privat communication
- [47] Pancheshnyi S, Starikovskaia S and Starikovskii A 1998 *Chemical Physics Letters* **294** 523–527 ISSN 0009-2614 URL <https://www.sciencedirect.com/science/article/pii/S0009261498008793>

- [48] Gans T, Lin C C, Schulz-von der Gathen V and Döbele H F 2003 *Phys. Rev. A* **67**(1) 012707 URL <https://link.aps.org/doi/10.1103/PhysRevA.67.012707>
- [49] Kozlov K V, Brandenburg R, Wagner H E, Morozov A M and Michel P 2005 *Journal of Physics D: Applied Physics* **38** 518 URL <https://dx.doi.org/10.1088/0022-3727/38/4/003>
- [50] Hoder T, Bonaventura Z, Bourdon A and Simek M 2015 *Journal of Applied Physics* **117** 073302